Cathodoluminescence spectroscopy of free and bound excitons in chemical-vapor-deposited diamond

Lawrence H. Robins, Edward N. Farabaugh, and Albert Feldman
National Institute of Standards and Technology, Ceramics Division, Gaithersburg, Maryland 20899
(Received 30 April 1993)

Cathodoluminescence (CL) spectroscopy was used to study exciton recombination at temperatures from 80 to 280 K in undoped and boron-doped diamond particles grown by hot-filament chemical vapor deposition. Spectral lines due to free and bound excitons were observed in the near-band-gap region, 4.6–5.5 eV. (The band gap of diamond is at 5.49 eV.) In the undoped particles, free-exciton lines were observed at 5.27 and 5.12 eV. Another set of lines, not previously reported, was observed between 4.7 and 5.0 eV, with the most intense lines at 4.757, 4.832, and 4.950 eV. The latter set of lines is attributed to excitons bound to lattice defects, possibly dislocations. In the boron-doped particles, excitons bound to boron acceptors were found to dominate the near-band-gap CL spectrum at low temperature. The most intense acceptor-bound-exciton line is at 5.20 eV. In both boron-doped and undoped particles, the exciton lines were much less intense in {111} crystal-growth sectors than in {100} sectors. Quenching of the exciton luminescence due to nonradiative recombination is believed to be the cause of the reduced intensity in the {111} sectors. The temperature dependence of the intensities, peak positions, and peak widths of the exciton lines was examined. The free and acceptor-bound excitons in the boron-doped particles were found to be in thermal equilibrium with each other. In the undoped particles, the free and defect-bound excitons were not in thermal equilibrium; the higher-energy bound-exciton lines (at 4.832 and 4.950 eV) decreased more rapidly with increasing temperature than either the lowest-energy bound-exciton line (at 4.757 eV) or the free-exciton lines. This behavior is attributed to thermally activated transitions from the higher-energy bound-exciton states to the lowest-energy state. The full width at half maximum (FWHM) of the free-exciton line, W_{FE}, increased with temperature at about the rate predicted for excitations thermalized near the bottom of a parabolic energy band: $W_{FE}(T)=W_{FE}(0)+1.795kT$. The FWHM's of the defect-bound- and acceptor-bound-exciton lines also increased with temperature, but at slower rates than for the free exciton. The peak positions of the exciton lines increased slightly with increasing temperature.

I. INTRODUCTION

Luminescence spectroscopy is one of the most useful methods for the characterization of intrinsic and defect-related electronic states in diamond. A wide variety of luminescence centers have been identified in chemical-vapor-deposited,[1] high-pressure synthetic and natural[2] diamond, but only a few of these centers emit photons with energies in the near-band-gap region, approximately 4.6–5.5 eV. The highest-energy luminescence in diamond arises from electron-hole pairs and free excitons.[3,4] These states are intrinsic excitations of the perfect crystal, and are not associated with lattice defects or impurities. The minimum energy of an electron-hole pair in diamond, the band gap, is 5.49 eV. The energy that binds the electron to the hole in the free exciton is 0.08 eV; the minimum energy of a free exciton is thus 5.41 eV. Because diamond has an indirect band gap, luminescence from electron-hole pairs and free excitons requires the emission of one or more phonons for each photon. The most intense free-exciton luminescence line, at 5.27 eV, requires the emission of a 0.14-eV transverse-optic (TO) phonon.

The neutral boron acceptor in lightly boron-doped diamond gives rise to a bound-exciton state with a binding energy 0.05 eV greater than the binding energy of the free exciton, and a total energy above the ground state of 5.36 eV.[4] (Diamonds which contain less than 10^{18} cm^{-3}, or 6 ppm, uncompensated boron acceptors can be considered to be lightly boron doped.) The TO phonon line of the acceptor-bound exciton in lightly boron-doped diamond thus occurs at 5.22 eV. Another bound-exciton state, denoted the N9 center, has been observed in type-Ia natural diamonds.[5] The N9 center is thought to be an exciton bound to a multiple-nitrogen center. The N9 center gives rise to a strong zero-phonon luminescence line at 5.25 eV, as well as one-phonon, two-phonon, and three-phonon lines. The binding energy of the N9 center is thus 0.16 eV greater than the binding energy of the free exciton. The boron acceptor-bound exciton and the N9 center are apparently the only previously observed bound-exciton states in diamond.

Results are presented here of a study of the near-band-gap luminescence emitted by undoped and boron-doped diamond particles grown by hot-filament chemical vapor deposition (CVD), and its variation with temperature from 80 to 280 K. The most important result of this study is the observation of previously unobserved spectral lines in the undoped particles. Three to five distinct lines were observed, with energies between 4.7 and 5.0 eV (0.5 to 0.8 eV below the band gap). In addition to these new spectral lines, boron acceptor-bound-exciton lines were observed in the boron-doped particles, and free-exciton lines were observed in both undoped and boron-doped

particles. Similarities between the temperature dependence of the new spectral lines and the temperature dependence of the lines attributed to free and acceptor-bound excitons suggest that the new lines arise from excitons trapped at defects in the diamond lattice. We speculate that these defects are dislocations or dislocation clusters similar to those found to produce exciton luminescence in other wide-band-gap semiconductors, notably cadmium sulfide[6,7] (CdS) and zinc selenide[8,9] (ZnSe).

II. EXPERIMENTAL PROCEDURE

Nominally undoped diamond particles were grown in a bell-jar hot-filament CVD reactor, which has been described previously.[10] Deposition conditions were as follows: gas pressure, 5 kPa; gas mass flow rate, 50 SCCM (SCCM denotes cubic centimeter per minute at STP); gas composition, 0.5% CH_4, 99.5% H_2; substrate holder temperature, 750 °C; filament temperature, 1800 °C; substrate, {100} oriented silicon wafer with dimensions 1.0×0.5 cm; substrate surface preparation, none; deposition time, 48 h. Diamond particles with diameters of ~10 μm and possessing a variety of cubo-octahedral and multiply twinned growth habits were formed during this deposition. A continuous polycrystalline diamond film was grown on another silicon substrate, with dimensions 1×1 cm, during the same deposition. The latter substrate was rubbed with 1 μm size diamond powder before the deposition in order to create a high density of sites for diamond nucleation.

The boron-doped diamond particles were grown in a tube-furnace hot-filament CVD reactor,[11] modified for boron doping by the addition of a liquid bubbler. The bubbler was filled with a 2.5 g/L solution of B_2O_3 in ethanol at a temperature of ~23 °C. Argon gas entered the bubbler at a flow rate of 8 SCCM. The gas pressure over the bubbler was 49 kPa (or 0.51 atm). The gas mixture leaving the bubbler was combined with 100 SCCM of hydrogen; the resulting gas mixture was then admitted to the deposition chamber. Deposition parameters were as follows: gas pressure in the deposition chamber, 5 kPa; nominal substrate temperature (furnace temperature), 650 °C; filament temperature, 1800 °C; substrate, {100} oriented silicon, 1×1 cm; substrate surface preparation, none; deposition time, 68 h. Diamond particles with diameters of ~40 μm and a variety of growth habits were formed during the boron-doping deposition.

Cathodoluminescence (CL) was excited by a conventional scanning electron microscope that had been modified to perform CL imaging and spectroscopy. The specimen temperature could be set anywhere in the range from 79 to 320 K. The CL was detected by a grating spectrometer equipped with an optical multichannel detector. The CL apparatus has been described more fully previously.[12]

III. EXPERIMENTAL RESULTS

A. Low-temperature CL spectra

Preliminary examination of the undoped diamond specimen in the scanning electron microscope (SEM) showed that well-faceted cubo-octahedral particles with smooth surfaces give rise to the most intense near-band-gap CL. Several particles of this type were selected for more detailed characterization. A secondary-electron SEM micrograph of one of the selected undoped particles is shown in Fig. 1(a). This particle will be designated particle 1.

The {111} facets of the boron-doped particles invariably are rough and uneven as viewed in the SEM, but the {100} facets sometimes are smooth. Particles with smooth {100} facets were found to give rise to the most intense near-band-gap CL. Several particles of this type were selected for more detailed examination. A secondary-electron micrograph of one of the selected boron-doped particles is shown in Fig. 1(b). This particle will be referred to as particle 2.

Near-band-gap CL spectra from {100} and {111} growth sectors of particle 1, taken at $T=80$ K, are plotted in Fig. 2(a). Seven resolved or partially resolved spectral lines are designated A1–G1 in Fig. 2(a). Two lines can be identified with free-exciton recombination: A1 at 5.264 eV, attributed to the emission of a transverse-optic phonon together with the photon, and B1 at 5.121 eV attributed to the emission of two phonons. The five lower-energy lines, C1 at 4.950 eV, D1 at 4.920 eV, E1 at 4.832 eV, F1 at 4.798 eV, and G1 at 4.757 eV, have not, to our

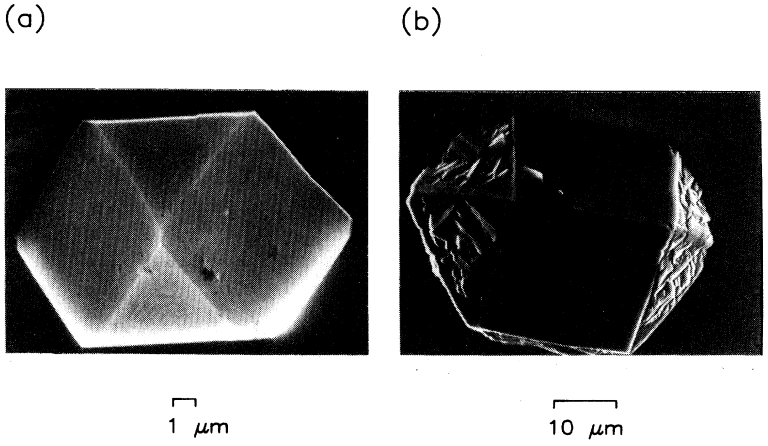

FIG. 1. (a) SEM micrograph of an undoped diamond particle grown by hot-filament CVD, designated particle 1. (b) SEM micrograph of a boron-doped diamond particle grown by hot-filament CVD, designated particle 2.

knowledge, previously been reported in any type of diamond. These lines are tentatively attributed to excitons bound to lattice defects, and will thus be denoted the defect-bound-exciton lines.

The intensity of the exciton CL is significantly lower from the {111} growth sector than from the {100} growth sector of particle 1. The intensity of the CL spectrum taken from the {111} sector has been multiplied by a factor of 4.3 to enhance its visibility in Fig. 2(a). This factor was chosen to make the plotted intensities of the lowest-energy bound-exciton line (G1) equal in both spectra. It can be seen in Fig. 2(a) that the intensity reduction on going from the {100} to the {111} sector is proportionately much greater for the free-exciton lines than for the bound-exciton lines. The free-exciton lines are barely discernible above the noise in the {111} spectrum.

The relative intensities of the bound-exciton lines (C1–G1) do not all decrease by the same factor on going from the {100} to the {111} sector. C1 is reduced most and D1 and F1 are reduced least. In fact, D1 and F1 are well resolved only in the {111} spectrum. D1 cannot be seen in the {100} spectrum, and F1 is only partially resolved (as a shoulder on the low-energy side of E1). The full widths at half maximum (FWHM's) of the bound-exciton lines also differ slightly between the {100} and {111} sectors.

The CL spectrum from a 24×30-μm region of the continuous polycrystalline film is shown in Fig. 2(b). As other researchers have reported, the intensity of the exciton CL is much lower from the polycrystalline film than from isolated particles;[13] the CL spectrum from the polycrystalline film has been multiplied by a factor of 50 to facilitate comparison with the spectra shown in Fig. 2(a). The free-exciton line designated A1 and the bound-exciton lines designated E1 and G1 are seen in Fig. 2(b). A1 is barely observable above the noise; E1 and G1 are somewhat better defined. Figure 2(b) demonstrates that the defect-bound-exciton states can occur in polycrystalline

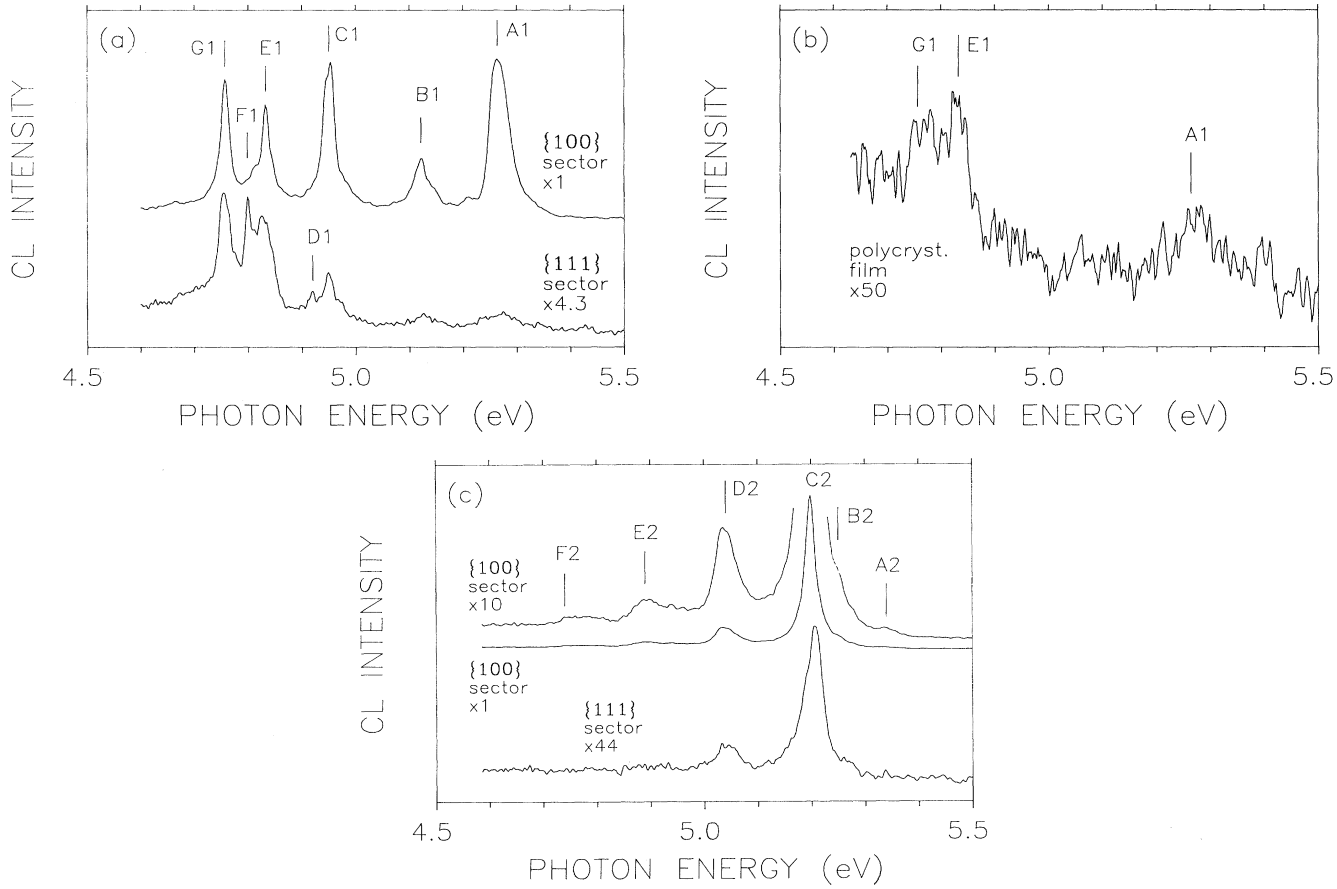

FIG. 2. (a) Near-band-gap CL spectra from {100} and {111} growth sectors of particle 1, $T=80$ K. The intensity of the {111} spectrum has been multiplied by a factor of 4.3 with respect to the {100} spectrum. The peak positions of the lines designated A1–G1 are 5.264, 5.121, 4.950, 4.920, 4.832, 4.798, and 4.757 eV, respectively. A1 and B1 are free-exciton lines, C1–F1 are bound-exciton lines. (b) Near-band-gap CL spectrum from continuous polycrystalline film, $T=80$ K. The intensity has been multiplied by a factor of 50 with respect to part (a). (c) Near-band-gap CL spectra from {100} and {111} growth sectors of particle 2 (boron-doped), $T=80$ K. The intensity of the {111} spectrum has been multiplied by a factor of 44 with respect to the {100} spectrum. The peak positions of the lines designated A2–F2 are 5.34, 5.25, 5.20, 5.04, 4.89, and 4.74 eV. B2 is due to free excitons; the other lines are due to boron acceptor-bound excitons.

diamond as well as in isolated diamond particles, although the luminescence efficiency is considerably lower in the polycrystalline film.

Near-band-gap CL spectra from {100} and {111} growth sectors of particle 2, taken at $T=80$ K, are plotted in Fig. 2(c). At least six lines can be resolved in the spectrum from the {100} sector. Five of these lines have been identified as arising from the recombination of boron acceptor-bound excitons.[4] The weak line at 5.34 eV, A2, is the zero-phonon line of the acceptor-bound exciton; C2, the intense line at 5.20 eV, is due to the emission of a TO phonon together with the photon; D2 at 5.04 eV is due to the emission of two phonons; E2 at 4.89 eV is due to the emission of three phonons; and F2 at 4.74 eV is due to the emission of four phonons. Line B2, at ~ 5.25 eV, is attributed to free-exciton recombination with the emission of a TO phonon. (Line B2 in the boron-doped film thus arises from the same transition as A1 in the undoped film.) Line B2 is difficult to observe in Fig. 2(c) because of its low intensity and small separation from C2. It will be shown, however, that the intensity ratio of B2 to C2 increases with increasing temperature, and that B2 becomes readily observable at temperatures higher than 150 K.

Previous studies have found that in lightly boron-doped diamond, the principal free-exciton line occurs at 5.27 eV, the same energy as in undoped material, and the principal acceptor-bound-exciton line occurs at 5.22 eV.[4] (These are both TO phonon lines.) In particle 2, the principal free-exciton line (B2) occurs at ~ 5.25 eV and the principal acceptor-bound-exciton line (C2) occurs at 5.20 eV. The free- and bound-exciton lines in particle 2 are thus shifted down in energy by 0.02 eV from their positions in lightly boron-doped diamond. Similar band-gap-narrowing effects have been observed for interband optical transitions in other heavily doped semiconductors.[14]

The intensity of the acceptor-bound-exciton CL is much lower from the {111} growth sector than from the {100} sector of particle 2. The intensity of the CL spectrum from the {111} sector is multiplied by a factor of 44 to enhance its visibility in Fig. 2(c). This factor was chosen to make the plotted intensities of the main acceptor-bound-exciton line, C2, equal in both spectra.

CL spectra in the 1.5–3.5 eV region are plotted in Figs. 3(a) and 3(b). The luminescence in this spectral region arises from defects and impurities that possess low-energy excited states (compared to the band-gap energy of 5.49 eV). Figure 3(a) shows spectra from the {100} and {111} growth sectors of particle 1. Four components are observed in these spectra. Component A3 is a zero-phonon line at 2.156 eV, with associated phonon sidebands at lower energy, attributed to a complex that contains two atomic vacancies and one nitrogen atom (*V*-N-*V* center); component B3 is a zero-phonon line at 2.326 eV, with weak phonon sidebands, attributed to a nitrogen-related center; component C3 is a line at 2.48 eV, due to a defect of unknown structure; and component D3 is a broad band centered at 2.85 eV, attributed to dislocation-related defects. (The origins of components A3, B3, and D3 have been discussed previously.[12,15]) In these particles, components A3 and B3 are much stronger from the {100} sector than from the {111} sector; C3 is much stronger from the {111} sector; and D3 is somewhat stronger from the {111} sector. The CL spectrum from the {111} sector is multiplied by a factor of 0.61 in Fig. 3(a) to make the plotted intensities of D3 equal in both spectra.

Figure 3(b) shows defect CL spectra from the {100} and {111} sectors of particle 2. The spectrum from the {100} sector can be deconvoluted into two broad bands: band A4, with a peak position of 2.27 eV and FWHM of ~ 0.66 eV; and band B4, with a peak position of 3.09 eV and FWHM of ~ 0.66 eV. In the spectrum from the {111} sector, the peak position of band A4 is shifted down to 2.23 eV and B4 is not observed. A broad band similar to A4, with a peak position between 2.1 and 2.3 eV, is usually observed in the CL spectra of boron-doped

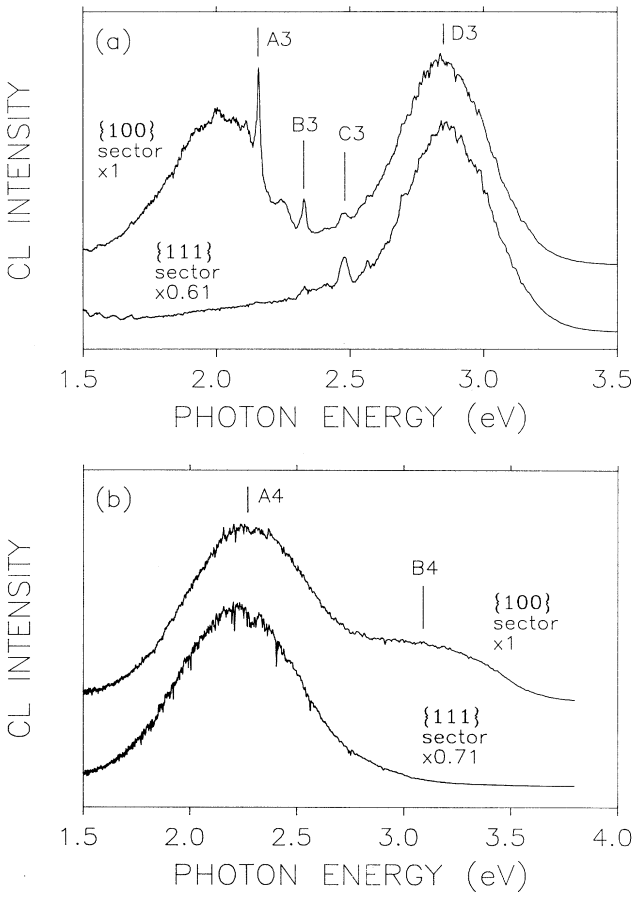

FIG. 3. (a) Visible-region CL spectra from {100} and {111} growth sectors of particle 1, $T=80$ K. The {111} spectrum has been multiplied by a factor of 0.61 with respect to the {100} spectrum. The peak positions of the lines designated A3–C3 are 2.156, 2.326, and 2.48 eV; the peak position of D3, the broad bell-shaped band, is 2.85 eV. (b) Visible-region CL spectra from {100} and {111} growth sectors of particle 2 (boron-doped), $T=80$ K. The intensity of the {111} spectrum has been multiplied by a factor of 0.71 with respect to the {100} spectrum. The peak position of band A4 is 2.27 eV (2.23 eV in the {111} sector); the peak position of band B4 is 3.1 eV.

diamonds. The intensity of the CL spectrum from the {111} sector has been multiplied by a factor of 0.71 in Fig. 3(b) to make the plotted intensities of A4 equal in both spectra. Spatially resolved CL spectra were also taken from the {100} and {111} growth sectors of several other undoped and boron-doped diamond particles. These spectra were similar to the spectra plotted in Figs. 2 and 3.

B. Temperature dependence: CL spectra

The temperature dependence of the near-band-gap CL from the {100} growth sector of particle 1 is displayed in Fig. 4(a). The spectra plotted in Fig. 4(a) were recorded at 14 temperatures from 80 to 276 K, where the ratio of adjacent temperatures is approximately constant. It can be seen in the figure that the intensities of the main free-exciton line, designated A1, and the lowest-energy bound-exciton line, designated G1, decrease rapidly with increasing temperature above ~150 K. The FWHM's of these lines increase with increasing temperature. The bound-exciton lines designated C1–F1 decrease more rapidly with increasing temperature than A1 or G1 and are virtually unobservable above 220 K. The temperature dependence of the near-band-gap CL from the {100} sector of another undoped particle, designated particle 3, was also examined in detail. The temperature dependence observed for particle 3 was very similar to that observed for particle 1. For conciseness, the complete set of temperature-dependent spectra from particle 3 will not be plotted here; the temperature dependencies of some of the important spectral parameters (integrated intensities, peak positions, and FWHM's) will, however, be plotted both for particle 1 and for particle 3.

The temperature dependence of the near-band-gap CL from the {100} growth sector of boron-doped particle 2 is displayed in Fig. 4(b). The temperatures were the same as in Fig. 4(a), except for the highest temperature (276 K), which was omitted. The intensities of the acceptor-bound-exciton lines decrease rapidly with increasing temperature above ~125 K. The intensity of the free-exciton line, designated B2, also decreases with increasing temperature, but not as rapidly as the acceptor-bound-exciton lines. The free-exciton line thus becomes more prominent with increasing temperature.

To better display the high-temperature data, the spectra recorded at temperatures above 200 K are replotted on expanded intensity scales in Fig. 5. Spectra from particle 1, recorded at temperatures between 207 and 276 K, are plotted in Fig. 5(a); spectra from particle 2, recorded at temperatures between 207 and 251 K, are plotted in Fig. 5(b). Weak lines are observed at ~4.98, ~4.82, and ~4.66 eV in the high-temperature spectra from particle 2. These lines are labeled A5, B5, and C5, respectively, in Fig. 5(b). The intensities of lines A5–C5 do not vary noticeably in the temperature range shown in this figure (207–251 K). It is likely that lines A5–C5 occur with similar intensity at lower temperatures also, but are difficult to observe at the lower temperatures because they are masked by the acceptor-bound-exciton lines C2–F2.

C. Temperature dependence: intensities of exciton lines

In order to quantitatively characterize the temperature dependence of the near-band-gap CL, it is useful to examine the temperature dependence of the integrated intensities, peak photon energies, and FWHM's of the various spectral lines. To obtain numerical values for these parameters, the spectra were fitted to a model line-shape function, which is discussed in the Appendix.

The spectrally integrated intensities of the exciton lines from particles 1–3 are plotted as functions of reciprocal temperature (T^{-1}) in Figs. 6–9. Figures 6, 7, and 9 use a logarithmic scale for the vertical (intensity) axis. The temperature dependence thus appears linear in these plots when it follows the thermally activated form

$$I(T)=I(0)e^{-\Delta E/kT} . \tag{1}$$

Note that the slope of the $\log(I)$ vs T^{-1} plot is *negative* when the intensity *increases* with increasing temperature and *positive* when the intensity *decreases* with increasing temperature.

The temperature dependence of the integrated exciton intensities from particle 2 is shown in Fig. 6. Three sets of data are plotted in Fig. 6(a): the free-exciton intensity (circles), the acceptor-bound-exciton intensity (squares),

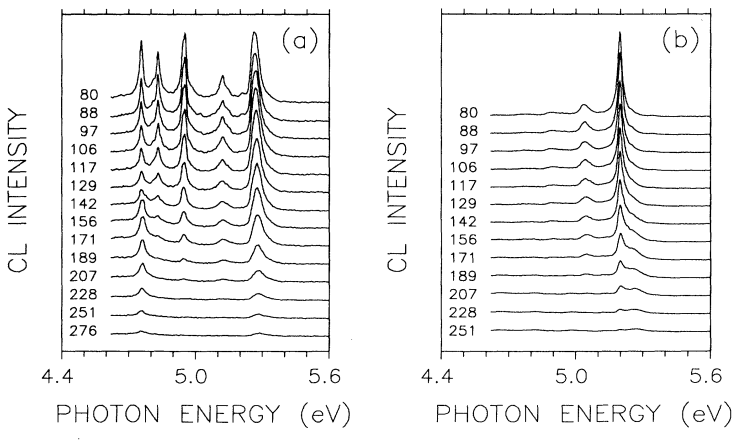

FIG. 4. Near-band-gap CL spectra of CVD diamond particles measured at temperatures from 80 to 276 K. (a) Particle 1, {100} growth sector. (b) Particle 2, boron-doped, {100} growth sector.

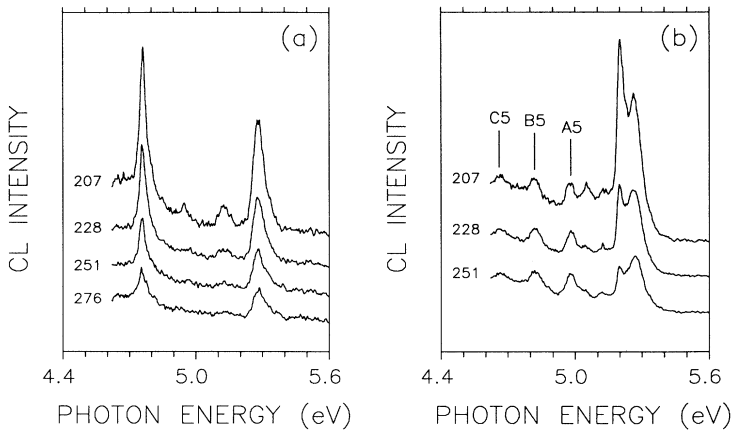

FIG. 5. Near-band-gap CL spectra of CVD diamond particles at temperatures above 200 K. (a) Particle 1, spectra taken at 207, 228, 251, and 276 K. (b) Particle 2, spectra taken at 207, 228, and 251 K. The peak positions of the lines designated A5, B5, and C5 are 4.98, 4.82, and 4.66 eV, respectively.

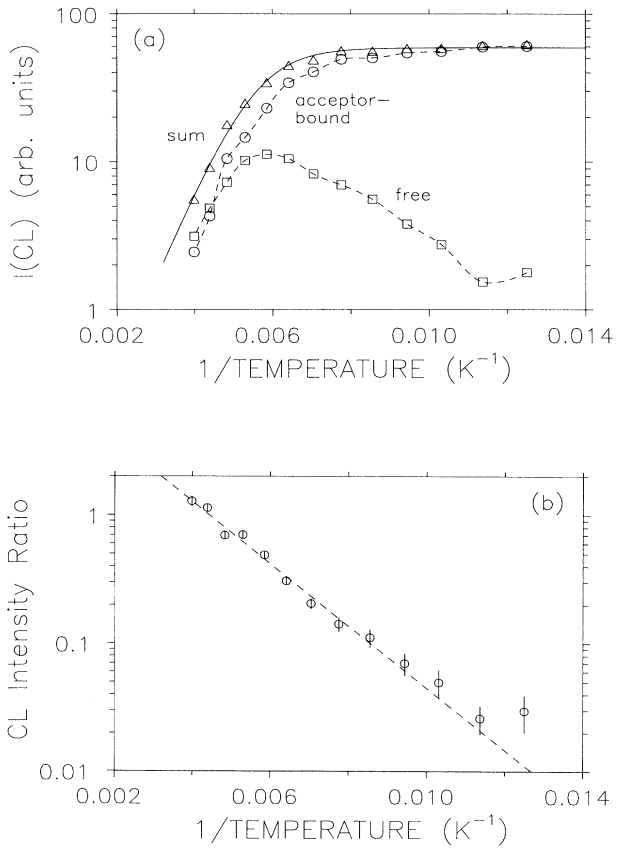

FIG. 6. (a) Temperature dependence of the integrated CL intensities from particle 2. Circles—free exciton; squares—acceptor-bound exciton; triangles—sum of free and acceptor-bound excitons. The dashed curves are guides to the eye. The solid curve represents the best fit of the function $I(T)=I(0)/[1+q\exp(-E_q/kT)]$ to the summed data (triangles). (b) Temperature dependence of the intensity ratio $I_{\text{free}}/I_{\text{acceptor-bound}}$. The straight line represents the best fit of the function $R(T)=R(\infty)\exp(-\Delta E/kT)$ to the data.

and the sum of the free- and acceptor-bound-exciton intensities (triangles). The curves drawn through the first two sets of data have no theoretical significance. The curve drawn through the summed data was obtained by fitting the function

$$I_{\text{CL}}(T)=\frac{I(0)}{1+qe^{-E_q/kT}} \tag{2}$$

to the data. This function approaches a constant at low temperature (or high reciprocal temperature) and approaches the thermally activated form of Eq. (1) at high temperature. The best fit to the data was obtained with parameter values $q=2400\pm400$ and $E_q=0.120\pm0.003$ eV.

The ratio of the free-exciton intensity to the acceptor-bound-exciton intensity is plotted vs T^{-1} in Fig. 6(b). The line drawn through the data is a fit to the function for a thermally activated process,

$$\frac{I_{\text{free}}(T)}{I_{\text{bound}}(T)}=Re^{-\Delta E/kT}. \tag{3}$$

The best first of Eq. (3) to the data is obtained with parameter values $R=11.9\pm1.3$ and $\Delta E=(4.82\pm0.16)\times10^{-3}$ eV.

The temperature dependencies of the integrated CL intensities from particles 1 and 3 are shown in Figs. 7(a) and 7(b), respectively. Three sets of data are plotted in each part of Fig. 7: the free-exciton intensity (circles); the total bound-exciton intensity, the sum of the intensities of lines C1-G1 (squares); and the sum of the free- and bound-exciton intensities (triangles). The dashed lines have no theoretical significance, but the solid lines, which represent the free-exciton curves, are fits to Eq. (2) with the following parameter values: $q=2100\pm300$, $E_q=0.115\pm0.002$ eV (particle 1); $q=1400\pm300$, $E_q=0.110\pm0.004$ eV (particle 3); $q=1800\pm200$, $E_q=0.113\pm0.002$ eV (weighted average of values from particles 1 and 3, weighted by σ^{-2} where σ is the uncer-

tainty in the value of each parameter). These values are very similar to the corresponding parameter values for the boron-doped particle.

It can be seen in Figs. 7(a) and 7(b) that the temperature dependence of the bound-exciton luminescence intensity is very similar to the temperature dependence of the free-exciton intensity. The bound-exciton intensity varies somewhat more with temperature than the free-exciton intensity at temperatures below 125 K, where the free-exciton intensity is virtually constant. Note also that the free-exciton intensity is lower and the bound-exciton intensity is higher for particle 3 than for particle 1; the relative variation of the intensities with temperature is, however, very similar for the two particles.

The temperature dependencies of the intensities of individual bound-exciton lines for particles 1 and 3 are plotted in Fig. 8. The lines are designated by the nomenclature of Fig. 2(a). Note that the intensity scales used in Fig. 8 are linear rather than logarithmic. Data from particle 1 are plotted in Fig. 8(a); data from particle 3 are plotted in Fig. 8(b). Note that the integrated intensity of line E1 includes the shoulder on the low-energy side of the main peak at 4.832 eV [see Figs. 2(a) and 4(a)]. It can be seen that G1 is the least intense of the three plotted lines at low temperature (except for the lowest temperature for particle 1, where lines G1 and E1 have approximately equal intensities) but the most intense at higher temperature. For both particles, there is a marked increase in the intensity of G1 from $T=120$ to 170 K, while C1 and E1 decrease monotonically with increasing temperature.

The intensity ratios of C1 and E1 to the total bound-exciton intensity (the sum of the integrated intensities of lines C1-G1) are plotted as functions of T^{-1}, on a logarithmic intensity scale, in Fig. 9. Data from particle 1 are plotted in Fig. 9(a); data from particle 3 are plotted in Fig. 9(b). The intensity ratios are approximately constant at temperatures below 125 K, but decrease rapidly with increasing temperature above 125 K. The smooth curves in Fig. 9 (solid curves for C1, dashed curves for E1) represent fits of Eq. (2) to the data. The following parameter values were obtained: $q=(1.1\pm0.6)\times10^4, E_q=0.131\pm0.015$ eV for line C1 in particle 1; $q=(1.4\pm0.6)\times10^5, E_q=0.156\pm0.013$ eV for

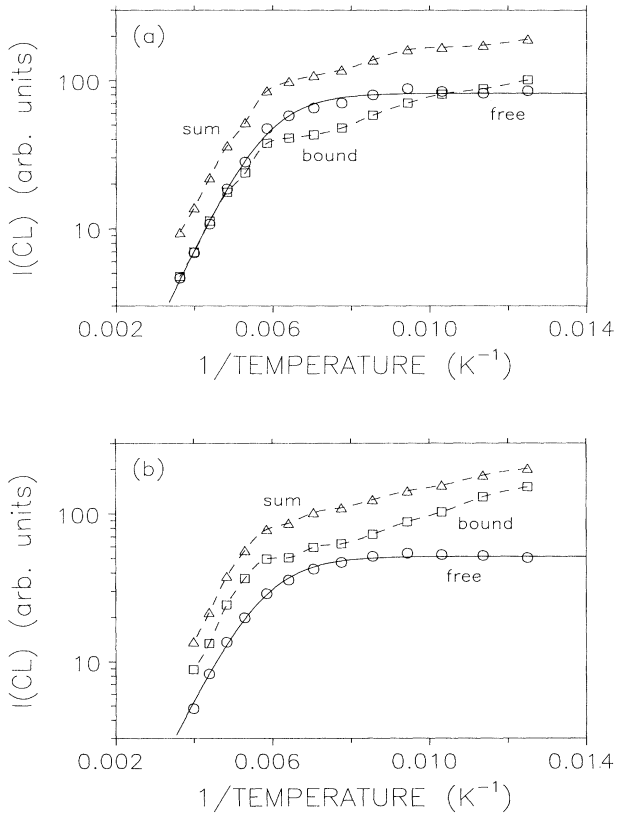

FIG. 7. (a) Temperature dependence of integrated CL intensities; data from particle 1. Circles—free exciton; squares—bound excitons; triangles—sum of free and bound excitons. The dashed curves are guides to the eye. The solid curve represents the best fit of the function $I(T)=I(0)/[1+q\exp(-E_q/kT)]$ to the free-exciton data (circles). (b) Temperature dependence of integrated CL intensities; data from particle 3. The data are plotted in the same way as in the previous plot.

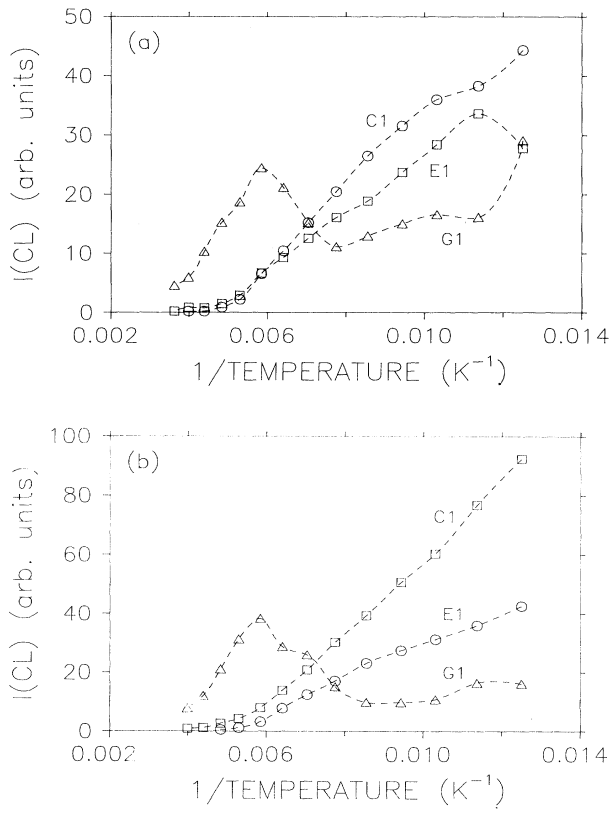

FIG. 8. (a) Temperature dependence of integrated intensities of bound-exciton lines; data from particle 1. Circles—C1 (4.950 eV); squares—E1 (4.832 eV); triangles—G1 (4.756 eV). The dashed curves are guides to the eye. (b) Temperature dependence of integrated intensities of bound-exciton lines; data from particle 3. The data are plotted in the same way as in the previous plot.

line C1 in particle 2; $q=530\pm240, E_q=0.091\pm0.015$ for line E1 in particle 1; and $q=580\pm180, E_q=0.081\pm0.005$ eV for line E1 in particle 2. The large uncertainties in the values of q reflect uncertainties in the extrapolation of the experimental data to infinite temperature ($T^{-1}=0$).

D. Temperature dependence: exciton linewidths and peak positions

The temperature dependencies of the FWHM's of the principal free- and bound-exciton lines are shown in Fig. 10. The temperature dependence of the FWHM of the main free-exciton line (A1) for particles 1 and 3 is plotted in Fig. 10(a) (circles for particle 1, squares for particle 3). The solid line in the figure represents the best fit to the data using the equation

$$W(T)=W_0+W_1kT\ . \tag{4}$$

The fitted parameters are $W_1=1.695\pm0.059$ and $W_0=30.4\pm0.7$ meV. The dashed line in Fig. 10(a)

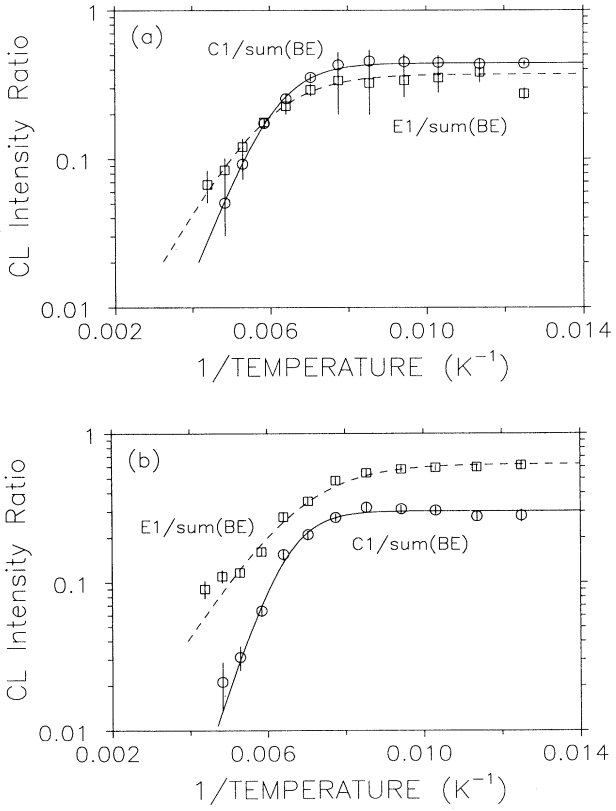

FIG. 9. (a) Temperature dependence of the intensity ratio of C1 to the sum of all the bound-exciton lines, and of the analogous intensity ratio for E1; data from particle 1. Circles with solid curve—C1. Squares with dashed curve—E1. The solid and dashed curves represent best fits of the function $I(T)=I(0)/[1+q\exp(-E_q/kT)]$ to the data. (b) Temperature dependence of the intensity ratio of C1 to the sum of all the bound-exciton lines, and of the analogous intensity ratio for E1; data from particle 3. The data are plotted in the same way as in the previous plot.

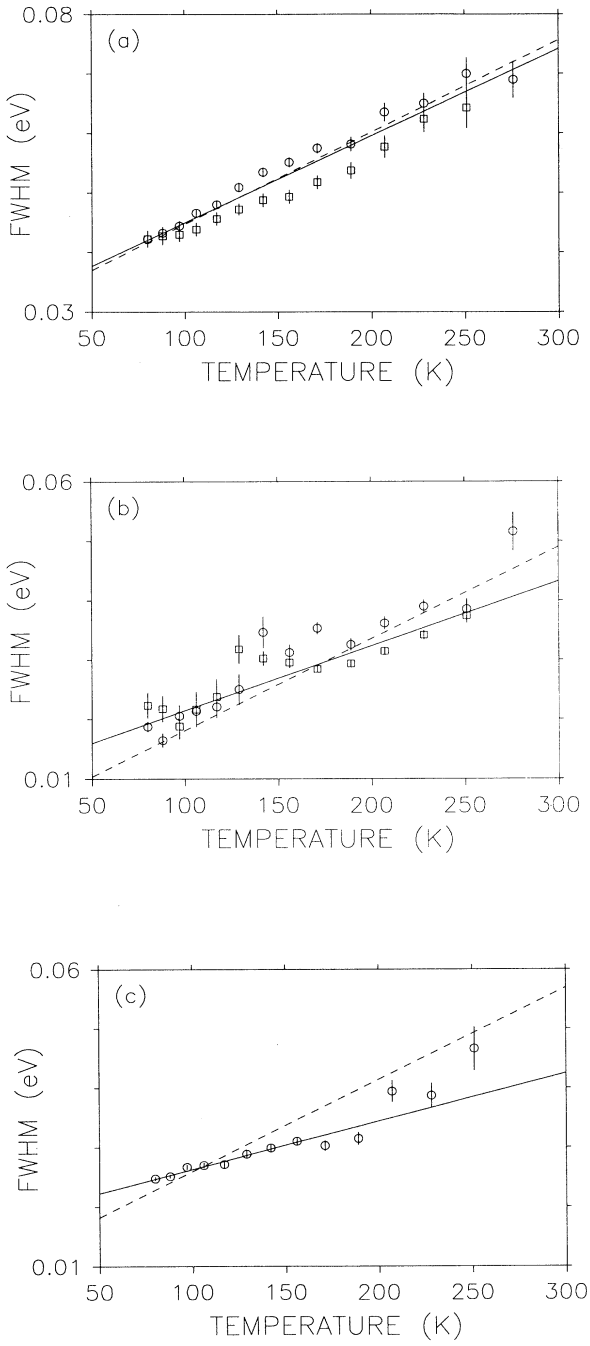

FIG. 10. (a) Temperature dependence of the FWHM of the principal free-exciton line (A1) for particles 1 and 3. Circles—particle 1; squares—particle 3. The solid line represents the equation $W(T)=1.695kT+30.4$ meV; the dashed line represents the equation $W(T)=1.795kT+29.2$ meV. (b) Temperature dependence of the FWHM of the lowest-energy bound-exciton line (G1) for particles 1 and 3. Circles—particle 1; squares—particle 3. The solid line represents the equation $W(T)=1.268kT+10.5$ meV; the dashed line represents the equation $W(T)=1.795kT+2.6$ meV. (c) Temperature dependence of the FWHM of the principal acceptor-bound-exciton line (C2) for particle 2. The solid line represents the equation $W(T)=0.939kT+18.2$ meV; the dashed line represents the equation $W(T)=1.795kT+10.5$ meV.

represents the best linear fit to the data with the slope W_1 fixed at 1.795; in this case, $W_0=29.2\pm0.2$ meV. (The significance of the value $W_1=1.795$ is explained in the Discussion section, below.) The temperature dependence of the FWHM of the lowest-energy bound-exciton line (G1) for particles 1 and 3 is plotted in Fig. 10(b). The solid line in Fig. 10(b) represents the best linear fit to the data, which gives parameter values $W_1=1.268\pm0.053$ and $W_0=10.5\pm0.8$ meV. The dashed line represents the best fit with W_1 fixed at 1.795, which gives $W_0=2.63\pm0.02$ meV. The temperature dependence of the FWHM of the one-phonon acceptor-bound-exciton line for particle 2 (line C2) is plotted in Fig. 10(c). The solid line in Fig. 10(c) represents the best fit to the data, which yields parameter values $W_1=0.939\pm0.056$ and $W_0=18.2\pm0.5$ meV, and the dashed line represents the best fit with W_1 fixed at 1.795, which yields $W_0=10.5\pm0.1$ meV.

The temperature dependencies of the peak positions of the principal free- and bound-exciton lines are shown in Fig. 11. The peak position of line A1 in particles 1 and 3 is shown in Fig. 11(a); the peak position of line G1 in particles 1 and 3 is shown in Fig. 11(b); and the peak position of line C2 in particle 2 is shown in Fig. 11(c). The dashed lines shown in Figs. 11(a)–11(c) are fits to the data using the equation

$$E_{\text{peak}}(T)=E_0+E_1kT\ , \tag{5}$$

with $E_1=0.5$. With E_1 fixed at 0.5, the low-temperature value of the peak position, E_0, is found to be 5.2663 ± 0.0001 eV for line A1, 4.7544 ± 0.0001 eV for line G1, and 5.1951 ± 0.0001 eV for line C2. The solid line show in Fig. 11(c) represents the best fit to the data with both parameters varied, which gives $E_1=0.329\pm0.020$ and $E_0=5.1966\pm0.0002$ eV.

There is a large amount of scatter in the peak position vs temperature data. In addition, the data points show a systematic deviation from the linear dependence given by Eq. (5). For all three lines represented in Fig. 11, the slopes of the experimental $E_{\text{peak}}(T)$ curves are seen to decrease with increasing temperature. This effect is especially noticeable for line E1, shown in Fig. 11(b); the peak position of E1 appears to reach a maximum between 150 and 200 K and then to decrease with increasing temperature above 200 K.

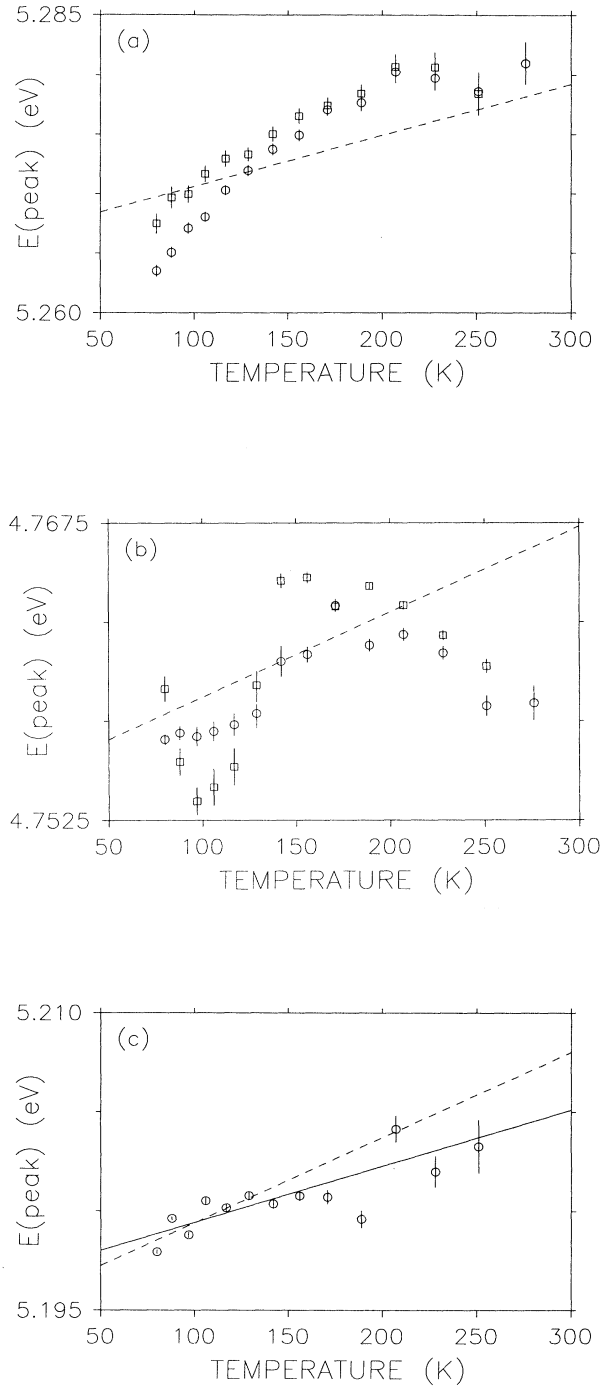

FIG. 11. (a) Temperature dependence of the peak position of the principal free-exciton line (A1) for particles 1 and 3. Circles—particle 1; squares—particle 3. The dashed line represents the equation $E_{\text{peak}}(T)=0.5kT+5.2663$ eV. (b) Temperature dependence of the peak position of the lowest-energy bound-exciton line (G1) for particles 1 and 3. Circles—particle 1; squares—particle 3. The dashed line represents the equation $E_{\text{peak}}(T)=0.5kT+4.7544$ eV. (c) Temperature dependence of the peak position of the principal acceptor-bound-exciton line (C2) for particle 2. The solid line represents the equation $E_{\text{peak}}(T)=0.329kT+5.1966$ eV. The dashed line represents the equation $E_{\text{peak}}(T)=0.5kT+5.1951$ eV.

IV. DISCUSSION

A. Spatial distribution of exciton CL

All of the exciton-related components of the CL are less intense in the {111} growth sectors than in the {100} growth sectors of the isolated particles, by factors ranging from 4 to 40. This is consistent with results reported previously for the free exciton.[13] What is the reason for this behavior? A simple model postulates that there exist nonradiative recombination centers capable of capturing both free and bound excitons, and the density of these nonradiative centers is higher in the {111} sectors than in the {100} sectors. This model can be developed further.

Because they are localized, bound excitons should be less susceptible to capture by the nonradiative centers than free excitons. As the exciton-defect binding energy increases, the extent of the bound-exciton wave function decreases, and the probability of capture by nonradiative centers decreases. The results shown in Figs. 2(a) and 2(c) are consistent with this model: the lower-energy defect-bound excitons are least likely to be captured by the nonradiative centers in the {111} sectors, the higher-energy defect-bound excitons (especially C1) are more likely to be captured, and the shallow acceptor-bound excitons and free excitons are the most likely to be captured.

According to Fig. 2(b), the exciton CL, both free and bound, is even more strongly quenched in the continuous film than in the {111} sector of an isolated particle. This implies a high concentration of nonradiative centers in the continuous film. There may be a correlation between this observation and the results of Raman spectroscopy, which show that continuous polycrystalline CVD diamond films typically have a higher nondiamond carbon content than isolated single-crystal particles grown under similar conditions.[16]

B. Temperature dependence: intensities of exciton lines

The temperature dependencies of the luminescence intensities plotted in Figs. 6–9 can be understood in terms of a model for the recombination of completely or partially thermalized groups of luminescent excited states. First, consider the recombination of the acceptor-bound and free excitons in particle 2. For conciseness, label the acceptor-bound-exciton state 1 and label the free-exciton state 2. We will show that the experimental results can be explained if we assume that the cross relaxation rates between 1 and 2 are faster than the corresponding decay rates to the ground state; i.e., states 1 and 2 are internally thermalized. Let the cross relaxation rates be $w_{12}(T)$ (from state 1 to state 2) and $w_{21}(T)$; let the rates for the generation of states 1 and 2 be G_1 and G_2; let the rates for radiative recombination (luminescence) be ν_{R1} and ν_{R2}; let the nonradiative recombination rates be $\nu_{N1}(T)$ and $\nu_{N2}(T)$; let the total recombination rates be $\nu_1(T)$ and $\nu_2(T)$ where $\nu_i(T)=\nu_{Ri}+\nu_{Ni}(T)$; and let the populations of the two states be n_1 and n_2. An energy level diagram to represent this model is shown in Fig. 12(a). The rate equations implied by this model are

$$\frac{dn_1}{dt}=G_1-[\nu_1(T)+w_{12}(T)]n_1+w_{21}(T)n_2 \tag{6}$$

and

$$\frac{dn_2}{dt}=G_2+w_{12}(T)n_1-[\nu_2(T)+w_{21}(T)]n_2\ . \tag{7}$$

The luminescence intensity from each state is the product of its population and radiative rate ($I_{L1}=\nu_{R1}n_1$). The luminescence intensities of the two states can be obtained by solving Eqs. (6) and (7) in the fast cross relaxation limit: $w_{21}(T)\gg\nu_2(T)$ and $w_{12}(T)\gg\nu_1(T)$. The quantities plotted in Fig. 6 are

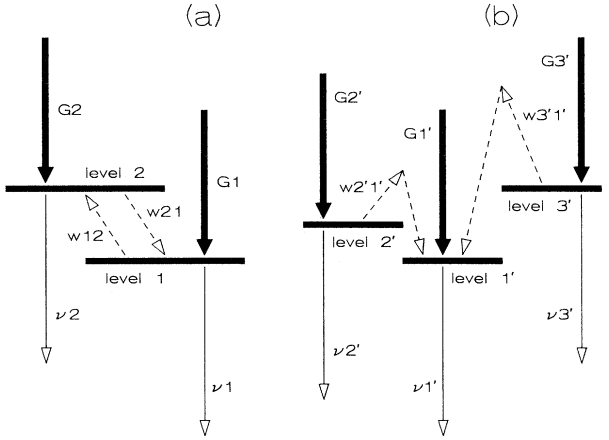

FIG. 12. (a) Energy level diagram used to interpret the temperature dependence of the exciton CL intensity in boron-doped diamond particles. In this diagram, level 1 represents the acceptor-bound exciton, level 2 represents the free exciton; $w_{12}(T)$ and $w_{21}(T)$ are cross-relaxation rates; G_1 and G_2 are generation rates; and $\nu_1(T)$ and $\nu_2(T)$ are recombination rates. (b) Energy level diagram used to interpret the temperature dependence of the bound-exciton CL intensity in undoped diamond particles. In this diagram, level 1′ represents the lowest-energy bound-exciton state; levels 2′ and 3′ represent higher-energy bound-exciton states; $w_{2'1'}(T)$ and $w_{3'1'}(T)$ are relaxation rates from the higher-energy states to the lowest-energy state (these rates are assumed to be thermally activated); $G_{1'}(T)$, $G_{2'}(T)$, and $G_{3'}(T)$ are generation rates; and $\nu_{1'}(T)$, $\nu_{2'}(T)$, and $\nu_{3'}(T)$ are recombination rates.

$$I_{L1}(T)+I_{L2}(T)=\frac{\nu_{R1}w_{21}(T)+\nu_{R2}w_{12}(T)}{\nu_1(T)w_{21}(T)+\nu_2(T)w_{12}(T)}\times(G_1+G_2) \tag{8}$$

and

$$\frac{I_{L2}(T)}{I_{L1}(T)}=\frac{\nu_{R2}w_{12}(T)}{\nu_{R1}w_{21}(T)}\ . \tag{9}$$

By detailed balance, the ratio of the cross relaxation rates is $w_{12}(T)/w_{21}(T)=\exp\{-\Delta E/kT\}$. The intensity ratio thus has the simple thermally activated form

$$\frac{I_{L2}(T)}{I_{L1}(T)}=\left[\frac{\nu_{R2}}{\nu_{R1}}\right]e^{-\Delta E/kT}\ . \tag{10}$$

This is precisely the form which was used to fit the intensity ratio data plotted in Fig. 6(b). According to the model of the luminescence process developed here, the prefactor $R=11.9\pm1.3$ is the ratio of the free-exciton radiative decay rate to the acceptor-bound-exciton radiative decay rate. Further, the fitted value of the activation energy, $\Delta E=(4.82\pm0.16)\times10^{-3}$ eV, is in good agreement with the observed splitting of ~0.05 eV between the free-exciton and acceptor-bound-exciton peaks in particle 2 [see Fig. 5(b)].

The experimentally observed decrease in the summed intensity with increasing temperature, shown in Fig. 6(a),

implies that the total recombination rates $\nu_1(T)$ and $\nu_2(T)$ increase with increasing temperature in a thermally activated manner, due to an increase in their nonradiative components. The experimental data can be explained by assuming that the nonradiative rates for states 1 and 2 have the same activation energy E_q and that the ratio of the nonradiative to the radiative rate is also the same for both states,

$$\frac{\nu_{Ni}(T)}{\nu_{Ri}}=qe^{-E_q/kT}, \quad \nu_i(T)=\nu_{Ri}(1+qe^{-E_q/kT}) \quad \text{for } i=1,2 . \tag{11}$$

The expression for the summed intensity, Eq. (8), then reduces to the form given by Eq. (2), which was used to fit the data in Fig. 6(a). The prefactor $q=2400\pm400$ is thus identified as the ratio of the nonradiative rates (in the high-temperature limit) to the radiative rates; $E_q=0.120\pm0.003$ eV is identified as the energy barrier which must be overcome for the excitons to recombine through the nonradiative channel.

Next, consider the recombination of the free and defect-bound excitons in particles 1 and 3. It was pointed out in the discussion of Fig. 7 that the temperature dependence of the free-exciton intensity for particles 1 and 3 is almost identical to the temperature dependence of the summed exciton intensity (free plus acceptor-bound) for particle 2. This implies that the temperature dependence of the free-exciton recombination rate in the undoped particles is similar to the temperature dependence of the free- and acceptor-bound-exciton recombination rates in the boron-doped particle. In other words, the temperature dependencies of the recombination rates and luminescence intensities are given by the equations

$$\nu(T)=\nu_R(1+qe^{-E_q/kT}) ,$$
$$I_L(T)=\frac{\nu_R}{\nu(T)}G=\frac{G}{1+qe^{-E_q/kT}} , \tag{12}$$

where q and E_q have the same values for the free excitons in particles 1–3 and for the acceptor-bound excitons in particle 2.

The temperature dependence of the intensities of the defect-bound-exciton lines is more difficult to explain. Figures 4(a) and 5(a) show that several defect-bound-exciton states luminesce with roughly equal intensities at low temperature, but that the lowest-energy state (G1) becomes dominant at high temperature. This is the opposite of what would be expected for a set of thermalized energy levels, in which the fraction of the total population in the higher levels increases monotonically with increasing temperature.

The experimental results for the defect-bound excitons can be explained by the following model. Label the lowest-energy level (corresponding to state G1) 1′ and label the higher-energy levels (corresponding to states E1 and C1) 2′ and 3′, respectively. Assume that relaxation can occur from 2′ to 1′, but than an energy barrier E_{b2} must be overcome for this relaxation to occur. Similarly, assume that relaxation from 3′ to 1′ can occur over an energy barrier E_{b3}. The relaxation rates $w_{3'1'}$, and $w_{2'1'}$ are thus thermally activated:

$$w_{j'1'}(T)=w^0_{j'1'}e^{-E_{bj'}/kT} \quad \text{for } j'=2',3' . \tag{13}$$

Assume that the reverse processes, transitions from 1′ to 2′ or 1′ to 3′, can be neglected. [By detailed balance, with $\Delta E_{1'2'}=0.076$ eV, the ratio of upward to downward transition rates is $w_{1'2'}(T)/w_{2'1'}(T)=0.04$ at 276 K, the highest temperature probed. Similarly, with $\Delta E_{1'3'}=0.194$ eV, $w_{1'3'}(T)/w_{3'1'}(T)=3\times10^{-4}$ at 276 K.] Let the generation rates of the three states be $G_{j'}(T)$ ($j'=1$ to 3), let the recombination rates be $\nu_{j'}(T)=\nu_{Rj'}+\nu_{Nj'}(T)$, and let the populations of the states be $n_{j'}$. The generation rates are assumed here to be temperature dependent, in contrast to the previous model. If the defect-bound excitons are generated by the capture of free excitons, then the generation rates should depend on the free-exciton population, which varies with temperature. An energy level diagram to represent this model is shown in Fig. 12(b). The rate equations implied by the model are

$$\frac{dn_{1'}}{dt}=G_{1'}(T)-\nu_{1'}(T)n_{1'}+w_{2'1'}(T)n_{2'}+w_{3'1'}(T)n_{3'} , \tag{14}$$

$$\frac{dn_{2'}}{dt}=G_{2'}(T)-[\nu_{2'}(T)+w_{2'1'}(T)]n_{2'} ,$$
$$\frac{dn_{3'}}{dt}=G_{3'}(T)-[\nu_{3'}(T)+w_{3'1'}(T)]n_{3'} . \tag{15}$$

These equations can be solved to obtain the steady-state luminescence intensities $I_{Lj'}=\nu_{Rj'}n_{j'}$,

$$I_{L1'}=\frac{\nu_{R1'}}{\nu_{1'}(T)}\left[G_{1'}(T)+\frac{w_{2'1'}(T)G_{2'}(T)}{\nu_{2'}(T)+w_{2'1'}(T)}+\frac{w_{3'1'}(T)G_{3'}(T)}{\nu_{3'}(T)+w_{3'1'}(T)}\right] , \tag{16}$$

$$I_{L2'}=\frac{\nu_{R2'}G_{2'}(T)}{\nu_{2'}(T)+w_{2'1'}(T)} \quad \text{and} \quad I_{L3'}=\frac{\nu_{R3'}G_{3'}(T)}{\nu_{3'}(T)+w_{3'1'}(T)} . \tag{17}$$

Two more assumptions are needed to explain the experimental results. First, assume that the nonradiative recombination rates are small compared to the radiative rates, so that $\nu_{j'}(T)\approx\nu_{Rj'}$. Second, assume that the generation rates $G_{j'}(T)$ are all proportional to a single temperature-dependent function, $G_{j'}(T)=g_{j'}G_0(T)$ where $g_{1'}+g_{2'}+g_{3'}=1$. If these relations are substituted into Eqs. (16) and (17), the sum of the luminescence intensities is found to be $\sum(I_{Lj'})=G_0(T)$. It was suggested above that the temperature dependence of the generation rates is determined mainly by the temperature dependence of the free-exciton population. If these assumptions are correct, then the total defect-bound-exciton intensity should have a similar temperature dependence to the free-exciton intensity. This prediction is supported by the data in Fig. 7.

The temperature dependence of the ratios $I_{L2'}/\sum(I_{Lj'})$

and $I_{L3'}/\sum(I_{Lj'})$ can be predicted by substituting the equations $\nu_{j'}(T)\approx\nu_{Rj'}$, $G_{j'}(T)=g_{j'}G_0(T)$, $G_0(T)=\sum(I_{Lj'})$, and Eq. (13) into Eq. (17). The expressions thus obtained are

$$\frac{I_{L2'}}{\sum I_{Lj'}}=\frac{\nu_{R2}g_{2'}}{\nu_{R2}+w_{2'1'}(T)}=\frac{g_{2'}}{1+(w^0_{2'1'}/\nu_{R2})e^{-E_{b2}/kT}},$$
$$\frac{I_{L3'}}{\sum I_{Lj'}}=\frac{g_{3'}}{1+(w^0_{3'1'}/\nu_{R2})}e^{-E_{b3}/kT}. \quad (18)$$

These expressions have the same functional form as Eq. (2), which was used to fit the observed temperature dependence of the ratios $I_{L2'}/\sum(I_{Lj'})$ and $I_{L3'}/\sum(I_{Lj'})$.

The fitted values of the energy barriers E_{b2} and E_{b3} (the weighted averages of the results from particles 1 and 3) are $E_{b2}=0.082\pm0.005$ eV and $E_{b3}=0.146\pm0.010$ eV. According to these results, the energy barrier to relaxation between levels 1′ and 2′ lies about as far above level 2′ (0.082 eV) as 1′ lies below 2′ (0.076 eV); similarly, the barrier to relaxation between 1′ and 3′ lies almost as far above level 3′ (0.146 eV) as 1′ lies below 3′ (0.194 eV).

C. Temperature dependence: exciton linewidths and peak positions

A simple theory predicts that the line shape of the free-exciton luminescence lines in an indirect-gap semiconductor such as diamond[4] is

$$I(E)=I_0[E-(E_G-E_{BX}-E_P)]^{1/2}e^{-E/kT} \quad \text{for } E>E_G-E_{BX}-E_P, \quad (19)$$

where E_G is the electron-hole band gap, E_{BX} is the exciton binding energy, and E_P is the energy of the coupled phonon. The line shape is the product of two factors, the transition probability for optical transitions between the exciton and the ground state, which is proportional to $[E-(E_G-E_{BX}-E_P)]^{1/2}$, and the Boltzmann distribution of exciton kinetic energies. (The line shapes for free-exciton absorption and luminescence in an indirect-gap semiconductor are the same as the corresponding line shapes for unbound electron-hole pairs in a direct-gap semiconductor. In both cases, the transition probability varies as the square root of the excess energy of the excited state above the threshold required for its formation.[17])

In Fig. 13, the experimental line shape of the principal free-exciton line (A1) is compared to the theoretical line shape at two distinct temperatures, 80 and 228 K. The theoretical line-shape functions (solid lines) were chosen to have the same peak intensities and peak positions as the experimental line shapes (dotted lines), but to have the FWHM's and line shapes determined by Eq. (19). The data presented in Fig. 13 are from particle 1. The experimental lines are seen to be broader than the theoretical lines, and also more symmetric, with a less abrupt low-energy threshold. The disagreement between the experimental and theoretical line shapes is, however, less pronounced at 228 K than at 80 K, especially towards high energy. Also, the thermal broadening of the experimental line from 80 to 228 K is seen to occur primarily on the high-energy side of the peak, in qualitative agreement with Eq. (19). These results suggest that the free-exciton line broadens and shifts to higher energy with increasing temperature, in accordance with Eq. (19), but that there are additional, nonthermal broadening mechanisms. The nonthermal broadening is responsible for the large free-exciton linewidth at low temperature.

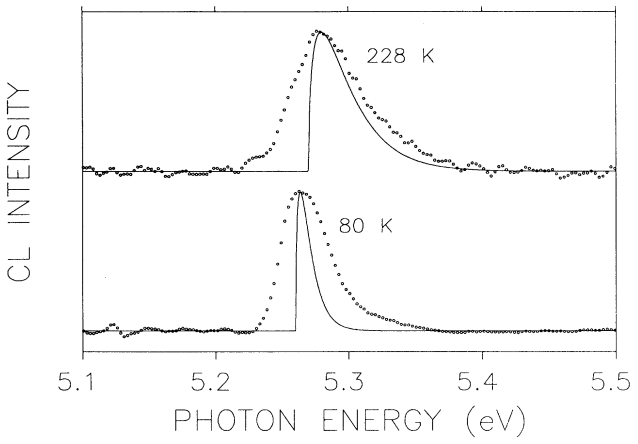

FIG. 13. Line shape of the principal free-exciton line (A1) in particle 1 at two temperatures, $T=80$ and 228 K. Experimental data (small circles) are compared with model line-shape functions $I(E)=I_0(E-E_{\text{threshold}})^{1/2}\exp(-E/kT)$ (solid lines), where the parameters I_0 and $E_{\text{threshold}}$ are chosen to make the peak intensities and peak positions of the model functions match the experimental data.

The temperature dependencies of the FWHM and peak position of the free-exciton line implied by Eq. (19) are

$$E_{\text{peak}}=E_G-E_{BX}-E_P+0.5kT \quad \text{and} \quad W=1.795kT. \quad (20)$$

If it is assumed that the experimental FWHM is the sum of the FWHM given by Eq. (20) and a temperature-independent term, then the linear function plotted as a dashed line in Fig. 10(a) is obtained. This function is seen to be in good agreement with the data. In Fig. 11(a), the peak position of the free-exciton line is seen to shift to higher energy with increasing temperature, in qualitative agreement with the model of Eqs. (19) and (20) (dashed line), although there is some discrepancy between the theory and the experimental results. The band gap of diamond is known to decrease with increasing temperature at high temperatures.[18] The latter effect should contribute a negative term to $E_{\text{peak}}(T)$ that increases in magnitude with increasing temperature, possibly explaining the decrease in the slope of the experimental curve at high temperature.

Next, consider the broadening of the bound-exciton lines with increasing temperature, which is shown in Figs. 10(b) and 10(c). Although the bound-exciton linewidths, which are indicated by the data points and solid lines in Figs. 10(b) and 10(c), increase with temperature at a slower rate than the free-exciton linewidths, the thermal broadening is still quite evident. The similarity

between the temperature-dependent linewidths of the defect-bound excitons in particles 1 and 3 [Fig. 10(b)] and the acceptor-bound excitons in particle 2 [Fig. 10(c)] suggests that the mechanism for the thermal broadening is the same in both systems. The theory that underlies Eqs. (19) and (20) cannot explain the thermal broadening of the bound-exciton lines. Bound excitons are localized at defect or impurity sites. The bound-exciton energy spectrum should therefore consist of discrete lines, rather than the parabolic bands characteristic of free excitons and other mobile excitations. Bound excitons in high-purity, defect-free crystalline semiconductors are known to give rise to very narrow, symmetric luminescence lines that do not broaden appreciably with increasing temperature.[19]

We propose the following model to explain the thermal broadening of the bound-exciton lines. Suppose that the energies of the bound excitons vary from site to site due to residual stresses or other spatially inhomogeneous effects, and that the width of this energy distribution is larger than the Boltzmann energy kT at the highest temperature. Suppose also that the excitons are able to hop between adjacent sites, so that each bound exciton visits several sites before it recombines. According to the principle of detailed balance, hopping from a higher-energy site to a lower-energy site is more probable than the reverse process by a factor $\exp[(E_1-E_2)/kT]$, where E_1 is the energy of the bound exciton in the higher-energy site and E_2 is the energy in the lower-energy site. The process of hopping between sites with inequivalent energies will thus tend to establish a Boltzmann distribution for the energies of the occupied sites, whose width will increase with increasing temperature, in accordance with the experimental results.

To summarize the last two sections, the temperature dependence of the exciton intensities provides evidence for complete thermalization between the free- and acceptor-bound-exciton states in the boron-doped particle, and for partial thermalization among the distinct defect-bound-exciton states in the undoped particles. The temperature dependence of the bound-exciton linewidths provides evidence for thermalization (i.e., establishment of a Boltzmann energy distribution) within inhomogeneously broadened bound-exciton lines in both the boron-doped and undoped particles.

D. Structural models for defect-bound excitons

Although the structure of the defects that bind the excitons in the undoped particles cannot be determined with certainty, it is likely that these defects are dislocations. CVD diamond specimens generally contain a high density of {111} planar defects, such as twin boundaries and stacking faults, which are expected to be bounded by dislocations.[20] One of the main visible luminescence bands, the broad violet band labeled D3 in Fig. 3(a), is thought to arise from point defects or impurities localized near dislocation cores.[12,15] In addition, luminescence from excitons bound to dislocations has been observed in the II-VI semiconductors cadmium sulfide (CdS) and cubic zinc selenide (ZnSe).

Dislocations were created in high-quality single crystals of CdS by the following methods of plastic deformation: four-point bending and indentation at high temperature[6] and uniaxial compression at low temperature.[7,21] New luminescence bands were observed after the dislocations were formed. The peak positions of the three most intense new bands at low temperature (4.2 K) were 2.430, 2.439, and 2.447 eV according to one study,[6] or 2.433, 2.437, and 2.445 eV according to the other study.[7] The peaks shift to lower photon energy with increasing temperature. The 2.445- or 2.447-eV band was also observed by optical absorption.[21] The large oscillator strength of this band, deduced from the magnitude of the absorption coefficient, confirms the excitonic character of the dislocation-related luminescence (because a nonexcitonic process, such as recombination between a dislocation-bound hole and a free electron, would have much smaller oscillator strength).

Thin films of cubic ZnSe, grown epitaxially on GaAs by metal-organic chemical vapor deposition, were characterized by cathodoluminescence transmission electron microscopy (TEM). High-resolution CL imaging in the TEM revealed that two defect luminescence bands, a narrow band at 2.60 eV and a broader band at 2.52 eV, occur only in the neighborhood of individual dislocations or cluster of dislocations.[8,9] These bands were particularly intense from dense clusters of dislocations.

It is interesting to compare the binding energy of the defect-bound and free excitons in diamond with the energies of the corresponding defect states in CdS and ZnSe. The band gap of CdS at low temperature (4.2 K) is 2.582 eV, and the free-exciton binding energy E_{BX} is 0.028 eV;[22] the minimum energy of a free exciton in CdS is thus 2.554 eV. Assume that the emission energies of the dislocation-bound excitons are the averages of the values cited above:[6,7] 2.446, 2.438, and 2.432 eV. The energies that bind the excitons to the dislocations are then 0.108, 0.116, and 0.122 eV. Expressed as multiples of E_{BX}, these energies are $3.9E_{BX}$, $4.1E_{BX}$, and $4.4E_{BX}$. The band gap of cubic ZnSe at low temperature is 2.835 eV, and E_{BX} is 0.02 eV;[23] the minimum energy of a free exciton in cubic ZnSe is thus 2.815 eV. The energies that bind the excitons to the dislocations in ZnSe are then 0.215 and 0.295 eV, or $10.8E_{BX}$ and $14.8E_{BX}$. In diamond, E_{BX} is 0.08 eV, the minimum energy of a free exciton is 5.41 eV, and the three most intense defect-bound-exciton lines (G1, E1, and C1) occur at 4.950, 4.832, and 4.757 eV. The exciton-defect binding energies are thus 0.460, 0.578, and 0.653 eV, or $5.8E_{BX}$, $7.2E_{BX}$, and $8.2E_{BX}$. (These binding energies were obtained with the assumption that C1, E1, and G1 are zero-phonon lines. Because of their highly localized nature, the defect-bound excitons should not be subject to the selection rules that suppress the zero-phonon transitions of the free exciton and shallow acceptor-bound exciton in diamond. The only previously studied defect-bound exciton in diamond, the N9 center, was found to give rise to strong zero-phonon lines. The defect-bound excitons investigated in the present study are more tightly bound than the N9 center.)

It can be concluded that the binding energies of the

defect-bound excitons in diamond, when expressed as ratios to E_{BX}, fall in the same range as the binding energies of the dislocation-bound excitons in CdS and ZnSe. This supports the dislocation model for the defect-bound excitons in diamond. The binding energies of both free and defect-bound excitons are larger in diamond than in the II-VI materials because the static dielectric constant is smaller (5.5 for diamond, vs 9.3 in CdS and 8.1 in ZeSe) (Refs. 22 and 23) and the effective mass of the exciton is larger.

As pointed out in the discussion of Figs. 4, 5, and 8, the intensities of the defect-bound-exciton lines in diamond have an unusual temperature dependence; several lines have similar intensities at low temperature, but the lowest-energy line becomes dominant at high temperature. This type of temperature dependence is not seen for the dislocation-bound excitons in CdS;[7] rather, in CdS, the lower-energy lines are quenched first with increasing temperature. The model illustrated by Fig. 12(b), according to which excitons can be transferred from the higher-energy bound states to the lowest-energy bound state by thermally activated hopping over energy barriers, may thus apply only to diamond. One possibility is that each bound-exciton line in the diamond specimens corresponds to a specific type of dislocation-related defect. If the distance between adjacent sites (the defects that bind the excitons) is small, because the overall dislocation density is high or the dislocations are associated in dense clusters, then thermally activated site-to-site hopping of the bound excitons might be expected to occur at a significant rate, as implied by the model.

V. CONCLUSION

Cathodoluminescence spectroscopy was used to study free and bound excitons in undoped and boron-doped diamond particles grown by hot-filament CVD. The near-band-gap CL of the undoped particles is attributed to free excitons and excitons bound to lattice defects, possibly dislocations. The main defect-bound-exciton lines are at 4.950, 4.832, and 4.757 eV. The exciton-defect binding energies are six to eight times the free-exciton binding energy (0.08 eV); similar relationships hold for dislocation-bound excitons in CdS and ZnSe. The near-band-gap CL of the boron-doped particles is attributed to free excitons and excitons bound to boron acceptors. In both undoped and boron-doped particles, the exciton lines are less intense in {111} growth sectors than in {100} sectors, by factors ranging from 4 to 40. The quenching of the exciton luminescence in the {111} sectors is attributed to nonradiative recombination. The temperature dependence of the exciton intensities shows that the free and acceptor-bound excitons in the boron-doped particles are in thermal equilibrium with each other throughout the 80–280-K range. In the undoped particles, the free and defect-bound excitons are not in equilibrium with each other. Thermally activated transitions occur from the higher-energy defect-bound excitons to the lowest-energy defect-bound exciton. The temperature dependence of the FWHM and peak position of the free-exciton line is consistent with a Boltzmann distribution of exciton kinetic energies. The temperature dependencies of the FWHM's of the defect-bound- and acceptor-bound-exciton lines suggests that the bound-exciton energy levels are inhomogeneously broadened and that thermalization occurs within each inhomogeneously broadened level.

APPENDIX

The model function utilized to fit the experimental CL spectra can be written as

$$I_{\mathrm{CL}}(E)=\sum_{i=1}^{M} I_{\mathrm{FE},i}(E)+\sum_{j=1}^{N} I_{\mathrm{BE},j}(E)+I_{\mathrm{backgr}}(E)\ , \quad \text{(A1)}$$

where E is the energy of the emitted photon, M is the number of free-exciton lines, and N is the number of bound-exciton lines. $I_{\mathrm{backgr}}(E)$ represents the broad background intensity that is seen to underlie the narrow lines in the CL spectrum. [We do not know the physical origin of $I_{\mathrm{backgr}}(E)$; this component of the model function is purely empirical.] The line shape of each free-exciton line is represented by a skewed Gaussian function

$$I_{\mathrm{FE},i}(E)=I_{P,i}e^{-\ln(2)X_i^2/(1+S_iX_i)}\ , \quad \text{(A2)}$$

where

$$X_i=\left[1+\frac{S_i^2}{16}\right]^{1/2}\frac{2(E-E_{P,i})}{W_i}\ , \quad \text{(A3)}$$

and where $I_{P,i}$ is the peak intensity of the free-exciton line, $E_{P,i}$ is the peak photon energy, W_i is the FWHM, and S_i is a dimensionless skewing factor.

Notice that the skewed Gaussian function has singular behavior at the point $X_i=-(S_i)^{-1}$. To avoid the singular point, the line-shape function is represented in the region $X_i<-0.8(S_i)^{-1}$ by a normal Gaussian, which is defined to have the same magnitude and slope as the skewed Gaussian at the point $X_i=-0.8(S_i)^{-1}$. The values of the fitted line-shape functions are close to zero in the region $X_i<-0.8(S_i)^{-1}$; this refinement therefore has little effect on the fitting procedure.

The line shape of each bound-exciton line is represented by the product of a Lorentzian and a Gaussian,

$$I_{\mathrm{BE},j}(E)=I_{P,j}\frac{1}{1+(2^{1-\lambda_j}-1)X_j^2}e^{-\ln(2)\lambda_jX_j^2}\ , \quad \text{(A4)}$$

where λ_j is a dimensionless parameter that varies between 0 for a pure Lorentzian line shape and 1 for a pure Gaussian. Good fits to the data were obtained with $\lambda_j=0.05$ for all the bound-exciton lines in the undoped diamond specimens, and with $\lambda_j=0.01$ for all the acceptor-bound-exciton lines in the boron-doped diamond specimen. The small values of λ_j indicate that the bound-exciton line shapes are close to pure Lorentzians.

Finally, the broad background that underlies the exci-

ton lines is represented by a cubic polynomial,

$$I_{\text{backgr}}(E)=I_{b,0}+I_{b,1}E+I_{b,2}E^2+I_{b,3}E^3 \ . \qquad \text{(A5)}$$

The model function given by Eqs. (A21)–(A25) was chosen because it fits the experimental spectra well. Notice that the integrated intensity of each exciton line is approximately equal to the product of its peak intensity and FWHM, $I_P W$, irrespective of the specific form of the line-shape function. Accurate values of the integrated intensities of the exciton lines were obtained by numerical integration.

[1]A. T. Collins, M. Kamo, and Y. Sato, J. Mater. Res. **5**, 2507 (1990).

[2]G. Davies, in *Chemistry and Physics of Carbon,* edited by P. L. Walker and P. A. Thrower (Dekker, New York, 1977), Vol. 13, pp. 1–143.

[3]P. J. Dean and I. H. Jones, Phys. Rev. **133**, A1698 (1964).

[4]P. J. Dean, E. C. Lightowlers, and D. R. Wight, Phys. Rev. **140**, A352 (1965).

[5]D. R. Wight and P. J. Dean, Phys. Rev. **154**, 689 (1967).

[6]V. D. Negrii and Y. A. Osip'yan, Fiz. Tverd. Tela (Leningrad) **20**, 744 (1978) [Sov. Phys. Solid State **20**, 432 (1978)].

[7]V. F. Grin, E. A. Salkov, N. I. Tarbaev, and Ga. A. Shepel'skii, Fiz. Tverd. Tela (Leningrad) **21**, 1690 (1979) [Sov. Phys. Solid State **970**, (1979)].

[8]S. Myhajlenko, J. L. Batstone, H. J. Hutchinson, and J. W. Steeds, J. Phys. C **17**, 6477 (1984).

[9]J. L. Batstone and J. W. Steeds, in *Microscopy of Semiconducting Materials, 1985,* Proceedings of the Royal Microscopical Society Conference, edited by A. G. Cullis and D. B. Holt, IOP Conf. Proc. No. 76 (Institute of Physics and Physical Society, London, 1985), pp. 383–388.

[10]E. N. Farabaugh and A. Feldman, in *Diamond, Silicon Carbide and Related Wide Bandgap Semiconductors,* edited by J. T. Glass, R. F. Messier, and N. Fujimori, MRS Symposia Proceedings No. 162 (Materials Research Society, Pittsburgh, 1990), pp. 127–132.

[11]E. N. Farabaugh, A. Feldman, L. H. Robins, and E. S. Etz, in *Diamond Optics,* edited by A. Feldman and S. Holly [Proc. SPIE **969**, 24 (1989)].

[12]L. H. Robins, L. P. Cook, E. N. Farabaugh, and A Feldman, Phys. Rev. B **39**, 13 367 (1989).

[13]H. Kawarada, Y. Yokota, and A. Hiraki, Appl. Phys. Lett. **57**, 1889 (1990).

[14]R. A. Abram, G. J. Rees, and B. L. H. Wilson, Adv. Phys. **27**, 799 (1978).

[15]L. H. Robins, E. N. Farabaugh, and A. Feldman, J. Mater. Res. **7**, 394 (1992).

[16]E. S. Etz, E. N. Farabaugh, A. Feldman, and L. H. Robins, in *Diamond Optics,* edited by A. Feldman and S. Holly [Proc. SPIE **969**, 86 (1988)].

[17]O. Madelung, *Introduction to Solid-State Theory* (Springer-Verlag, Berlin, 1978), pp. 266–284.

[18]C. D. Clark, P. J. Dean, and P. V. Harris, Proc. R. Soc. London Ser. A **277**, 312 (1964).

[19]P. J. Dean and D. C. Herbert, in *Excitons,* edited by K. Cho (Springer-Verlag, Berlin, 1979), pp. 55–182.

[20]D. Shechtman, E. N. Farabaugh, L. H. Robins, and A. Feldman, Proc. SPIE **1534**, 26 (1991).

[21]E. A. Sal'kov, N. I. Tarbaev, and G. A. Shepel'skii, Fiz. Tverd. Tela (Leningrad) **22**, 1110 (1980) [Sov. Phys. Solid State **22**, 646 (1980)].

[22]D. G. Thomas and J. J. Hopfield, Phys. Rev. **116**, 573 (1959).

[23]M. Aven, D. T. F. Marple, and B. Segall, J. Appl. Phys. Suppl. **32**, 2261 (1961).

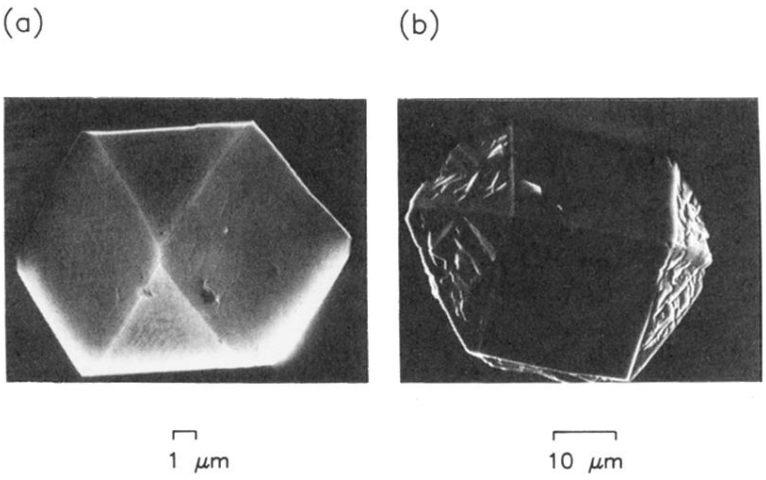

FIG. 1. (a) SEM micrograph of an undoped diamond particle grown by hot-filament CVD, designated particle 1. (b) SEM micrograph of a boron-doped diamond particle grown by hot-filament CVD, designated particle 2.